Available online at www.sciencedirect.com
SCIENCE DIRECT®
Journal of Sound and Vibration 290 (2006) 865–881
JOURNAL OF SOUND AND VIBRATION
www.elsevier.com/locate/jsvi

An induction motor model for high-frequency torsional vibration analysis

R.D. Widdle Jr.[a,*], C.M. Krousgrill Jr.[a], S.D. Sudhoff[b]

[a]*School of Mechanical Engineering, Purdue University, 1288 Mechanical Engineering Building, W. Lafayette, IN 47907-1288, USA*
[b]*School of Electrical and Computer Engineering, Purdue University, 1285 Electrical Engineering Building, W. Lafayette, IN 47907-1285, USA*

Received 30 April 2003; received in revised form 22 November 2004; accepted 28 April 2005
Available online 31 August 2005

Abstract

High-frequency torsional oscillations of a 50 horsepower (hp) induction motor are investigated up to approximately 30 kHz. It is experimentally determined that torsional oscillations, due to the switching harmonics of the motor drive, contribute significantly to the torsional oscillation of the output shaft. Two torsional vibration models are developed. One model assumes the rotor to be rigid, while the other has a compliant rotor. The compliant model allows for greater transmission of high-frequency oscillations, and a better prediction of the measured output shaft vibration.

1. Introduction

A typical induction motor is shown schematically in Fig. 1. The major components are the stator which remains stationary and the rotor which rotates the output shaft. An induction motor is operated by providing a balanced set of currents to windings in the stator. The currents produce a rotating magnetic field inside the motor. The rotating field induces current in the rotor, which then interacts with the magnetic field producing forces on the rotor, resulting in a net torque.

*Corresponding author. Tel.: +1 765 494 0232; fax: +1 765 494 0787.
E-mail address: widdlejr@ecn.purdue.edu (R.D. Widdle Jr.).

0022-460X/$ - see front matter © 2005 Elsevier Ltd. All rights reserved.
doi:10.1016/j.jsv.2005.04.026

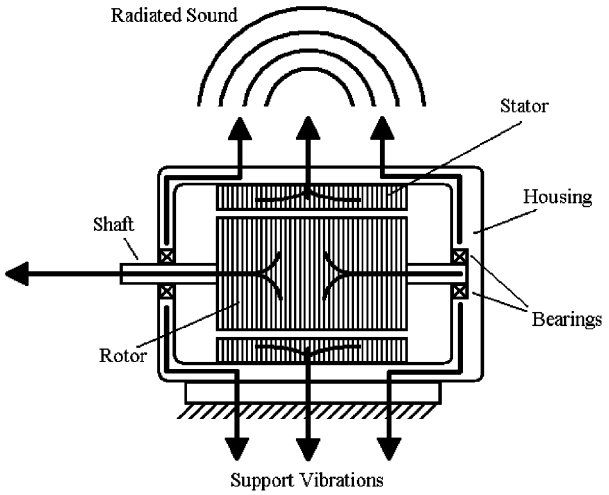

Fig. 1. Induction motor schematic and vibration transmission paths.

The speed of the motor is strongly dependent on the fundamental frequency of the current fed to the stator windings. Often solid-state inverters are used to alter the frequency of the power supply [1]. Some of the most common inverters consist of two components: an AC-to-DC rectifier and a DC-to-AC converter. Together they provided the ability to change the frequency of the power source. The DC-to-AC conversion involves switching the DC voltage in such a way that the inverter output approximates the desired waveform. Since the output is not an exact sinusoid, the signal contains harmonics of the switching frequency, in addition to the desired fundamental frequency component. These harmonics contribute to the excitation of the rotor, and are often in a frequency range considered to be high.

Several reasons exist for investigating the vibration of induction motors, and electric machinery in general. One is that, excessive vibration can lead to catastrophic mechanical failure [2]. Also, when a structure vibrates in a fluid medium sound is produced. Modern variable speed electric machines often produce unacceptably high levels of acoustic noise [3]. The noise can be irritating and can damage one's hearing. For naval applications, it is desirable to have the acoustic signature of onboard machinery as small as possible. Further, not only is it important to study noise in the audible frequency range for industrial and commercial use, but also in the high-frequency range for naval applications.

To model induction motor vibration, notice that vibration transmission through an induction machine can be thought of in terms of three paths, as illustrated in Fig. 1. The three paths are: electromagnetic excitation of the stator, transmission through the bearings, and oscillation down the shaft. Depending on the application, any of these transmission paths may be the source of unwanted acoustic radiation. For example, the shaft may drive equipment in the next room, or a propeller through a ships hull, making shaft oscillation mitigation a priority. The focus of this paper will be shaft torsional oscillations.

This investigation was motivated by the concern that high-frequency oscillations are transmitted through the hull of induction-motor-driven submarines, via the output shaft.

Consequently, the current study has two objectives. First, it is to be shown that high-frequency torsional oscillations, generated by the motor drive, are transmitted through the motor shaft. Second, a torsional vibration model is developed that will better approximate high-frequency torsional response.

The torsional vibration of induction machines has received considerable attention. Sheppard [2], Calonnec et al. [4], Wang et al. [5], and Hong and Sul [6] investigated torsional oscillation with an aim to analyze or predict mechanical failure in torsion. Perrin et al. [7] studied the torsional interaction of induction motors and reciprocating compressors, while Shadley et al. [8] employed a torsion model to study unstable self-excitation arising from speed–torque characteristics. Torsion, with respect to control strategies, has been studied by Kim et al. [9,10] and Mine et al. [11]. What all these investigations have in common is the use of a single rigid body to represent the rotor. This is an appropriate course of action when studying low-frequency vibration, since the rotor is likely behaving as a rigid body. However, at high frequencies compliancy of the rotor may be important.

This paper begins with a description of the experimental apparatus. Next, sample experimental results are presented showing the presence of high-frequency vibration components generated by the motor drive and transmitted to the motor output. Based on the geometry of the test apparatus, it continues with the development of two models used to describe the torsional vibration of an induction motor. The first model assumes compliancy of the rotor in torsion, and will be referred to as the compliant rotor model. The second model is a special case of the compliant rotor model; it assumes the rotor to be rigid, and will be referred to as the rigid rotor model.

2. Experiment

The aim in constructing the apparatus is to learn if high-frequency vibrations, excited by switching harmonics, are transmitted through the motor output shaft. Section 2.2 will give some sample experimental results indicating that this is the case.

2.1. Experimental apparatus

A schematic of the test apparatus appears in Fig. 2a. The test motor is a 50 horsepower (hp) induction motor manufactured by Baldor Motors and Drives. A torque transducer with high-frequency response, manufactured by Sensor Technology Ltd., is attached to the test motor with a coupling designed to electrically isolate the transducer from the motor. The optical rotary-type transducer has a frequency range of 0–10 kHz. It operates by modulating the intensity of a light beam as a function of torque. The transducer was selected in order to study high-frequency torsional oscillations of the shaft. The other couplings attaches the transducer to a flywheel. Throughout this paper, the hardware connecting torque transducers to adjacent components will be referred to as connection hardware.

As the mode number increases, in a structure with lumped masses or inertias, the most massive of the lumped elements become displaced less relative to the rest of the structure. Thus, for sufficiently high modes, the larger lumped elements may be considered to be stationary. For this

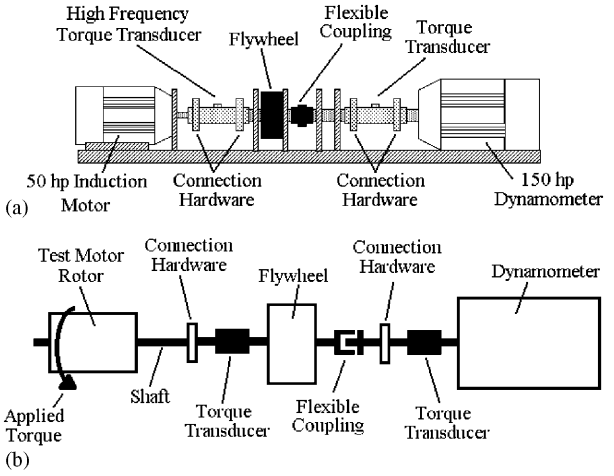

Fig. 2. (a) Schematic and (b) rotating components of the experimental apparatus.

reason the flywheel was added to the system; at high frequencies it is intended to mechanically isolate the test motor from the dynamometer.

Continuing down the shaft, the next element is a flexible coupling. This coupling is also intended to prevent the transmission of oscillation from one side of the test rig to the other. Next, another torque transducer and a 150 hp dynamometer follow the flexible coupling. The dynamometer and the adjacent torque transducer were manufactured by Dyne Systems.

A schematic of the rotating components of the experimental apparatus appears in Fig. 2b. The connection hardware connects the torque transducers to the shafts at either end. In the vibration models, the connection hardware joining the torque transducer to the flywheel is lumped with the flywheel. In addition, during the experiments discussed here the flywheel is held fixed. This will be considered when deriving the vibration models.

The rotor of the test motor is sketched in Fig. 3. It is composed of a number of steel laminations that are keyed and pressed onto a circular shaft. Aluminum bars, called rotor-bars, are imbedded in the laminations and run parallel to the shaft. A conductive plate, or end ring, goes over either end of the rotor, thereby electrically connecting all of the rotor-bars.

2.2. Sample experimental results

In this experiment the flywheel was prevented from rotating by attaching a mechanical stop, so that the shaft oscillation could be measured using accelerometers as described below. The motor was then excited using the motor drive. To determine the torque applied to the rotor, the currents and voltages supplied to the motor were recorded. After the experiment, the measurements were used to find the applied torque using an advanced induction motor model, developed by Sudhoff et al. [12,13]. The calculation was performed with a MATLAB routine, also provided by Sudhoff et al.

The induction motor model [12,13] is a new lumped parameter model, and is an improvement over the standard q–d model in that it is significantly more accurate in predicting switching

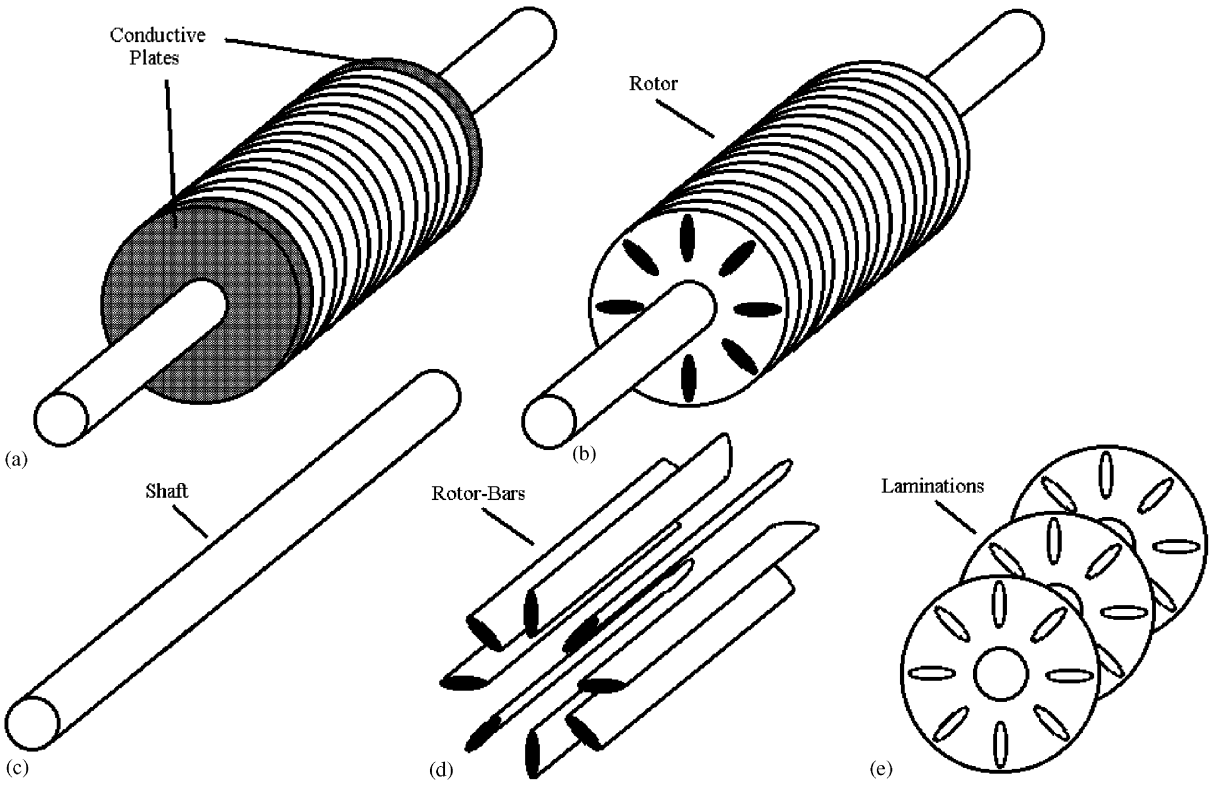

Fig. 3. Sketch of the rotor components: (a) rotor assembly, (b) rotor assembly without conductive plates, (c) shaft, (d) rotor-bars, and (e) rotor laminations.

frequency behavior. In particular, it predicts well the fundamental current component, average torque, and switching frequency torque ripple. The model is valid over a large operating range and is parameterized by a few laboratory tests.

Using the stationary rotor setup described above, the response of the connection hardware was measured using two accelerometers. The accelerometers were arranged on the connection hardware as shown in Fig. 4, with the rotation axis being in the z-direction. Accelerometer B was mounted such that the measured acceleration passed through the disk center. Accelerometer A measured acceleration parallel to B, but was displaced from the center by a distance $\rho_A = 0.046\,\mathrm{m}$. By assuming a small angular rotation, it can be shown that

$$\ddot{\theta} \approx \frac{1}{\rho_A}\left(a_{A,y} - a_{B,y}\right). \tag{1}$$

The measured torque is plotted as a function of frequency in Figs. 5a and 6a, for a fundamental frequency of 20 and 10 Hz, respectively, with a PWM duty cycle of 0.4. The corresponding measured angular acceleration is plotted as a function of frequency in Figs. 5b and 6b. One of the motivations for this study is to understand the ability of an induction motor to generate structure-borne sound. Acoustic radiation results from the fluctuating component of the motion. Thus, the

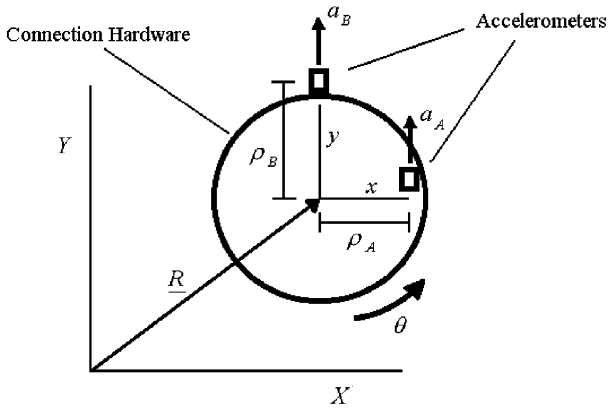

Fig. 4. Accelerometer arrangement on the connection hardware.

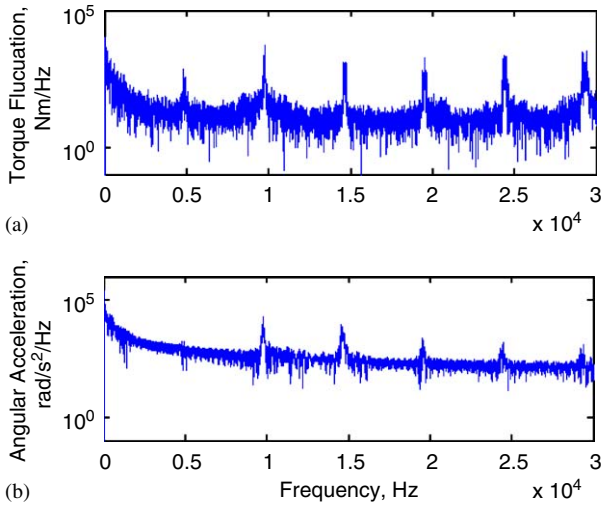

Fig. 5. (a) Fluctuating component of the measured input torque at the rotor and (b) measured angular acceleration at the connection hardware, with a fundamental frequency of 20 Hz.

mean value of the torque has been removed, and only the fluctuating component has been displayed in the figures.

Figs. 6 and 7 show that the fluctuating component of the input torque is dominated by switching harmonics. The switching harmonics appear as spikes at multiples of roughly 5 kHz. The figures also show that these frequency components also contribute significantly to the oscillation of the motor output shaft.

3. Modeling

Two torsional models are developed in this section. In order to compare the model with the fixed flywheel experiment, only components from the test motor up to the flywheel are included.

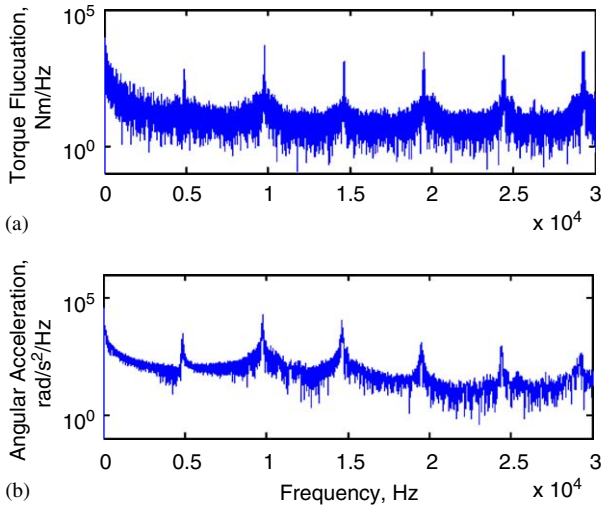

Fig. 6. (a) Fluctuating component of the measured input torque at the rotor and (b) measured angular acceleration at the connection hardware, with a fundamental frequency of 10 Hz.

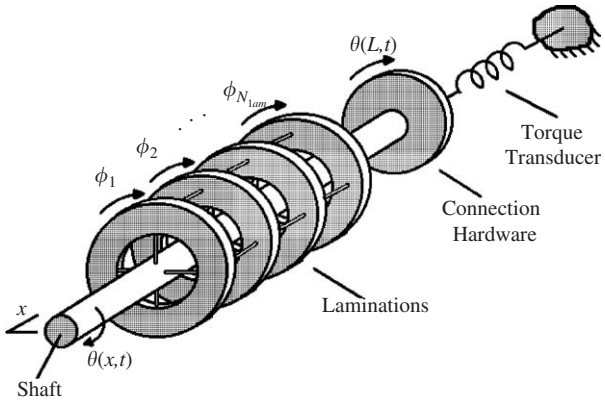

Fig. 7. Compliant rotor model of the test motor.

The first torsion model assumes a compliant rotor to account for high-frequency modes that involve its deformation. The second model assumes a rigid rotor.

3.1. Compliant rotor model

The compliant rotor model is intended to account for torsional deformation of the rotor. A drawing of the model appears in Fig. 7. The model consists of a compliant shaft and rigid annular disks, which represent the 480 laminations in the induction motor. The disks are connected to the shaft with effective torsional springs, representing compliancy of the actual laminations. The disks are also connected to each other with torsional springs representing the rotor-bars. The hardware that connects the motor to the torque transducer is lumped together as a rigid disk, while the

torque transducer is modeled as a torsional spring. The torque transducer is attached to the flywheel, and the flywheel is assumed to be stationary, since it was not allowed to rotate during the experiments. In other words, the torque transducer is grounded where it would attach to the flywheel. Also shown in Fig. 7 are $\theta(x,t)$, the angular displacement of the shaft, ϕ_1, the rotation of the ith lamination, and L, the length of the shaft.

The torsional stiffness of the springs representing the connection between the laminations and the shaft was found using the finite element analysis program ANSYS. The mesh used is shown in Fig. 8, and has approximately 40,000 degrees of freedom. Plane stress analysis is assumed here due to the thinness of the laminations.

To compute the torsional stiffness using finite elements, the slots that house the rotor-bars were fixed and a torque was applied to the inner surface of the lamination. To apply the torque, a pair of perpendicular forces was applied to each node on the inner surface such that the resultant force vector was tangent to the circle. This is shown in Fig. 9.

To describe the interaction of adjacent laminations via the rotor-bars, their deformation must be considered. Suppose two laminations have undergone a rotational displacement with respect to each other, then the deformation of the rotor-bar might look as shown schematically in Fig. 10. The segment of the rotor-bar, between the centers of the two laminations, is very short when compared to its width or depth. Therefore, it is assumed to deform in shear. Note that in the figure, the relative scale of h appears much larger than in the actual machine.

To derive the effective torsional stiffness, consider the segment of rotor-bar shown in Fig. 11. From mechanics of materials, the shear stress,τ, and shear strain, γ, are related by

$$\tau = G\gamma, \tag{2}$$

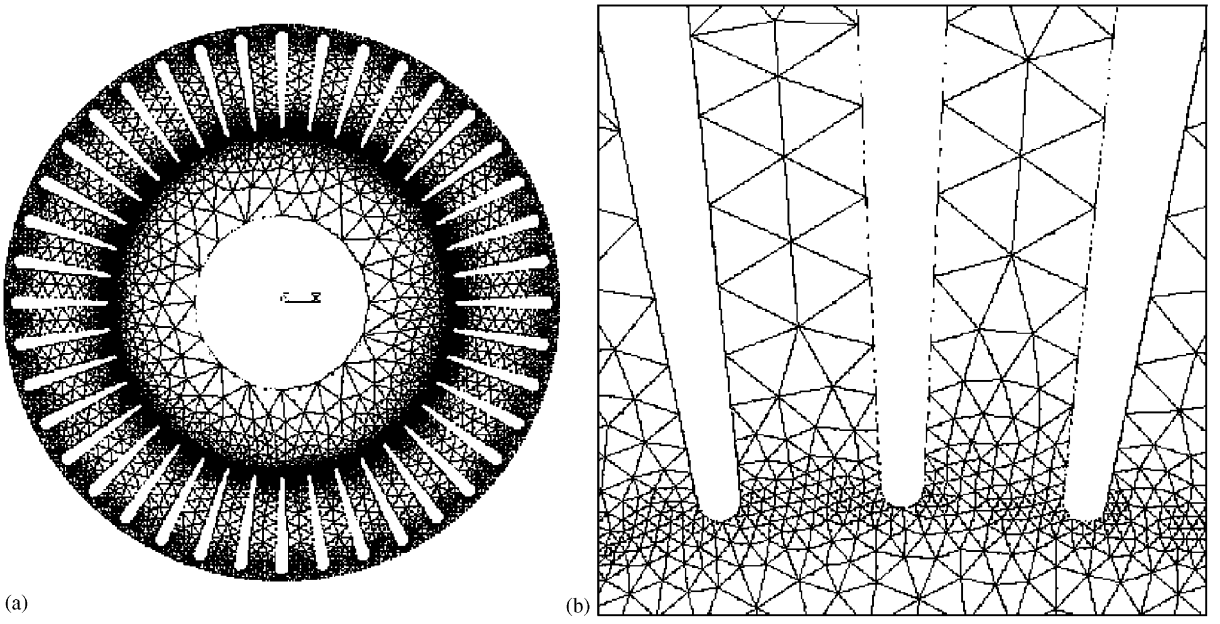

(a) (b)

Fig. 8. Finite element mesh used to find the stiffness of a lamination: (a) mesh for the entire lamination and (b) close-up of the mesh at the base of the rotor-bar slots.

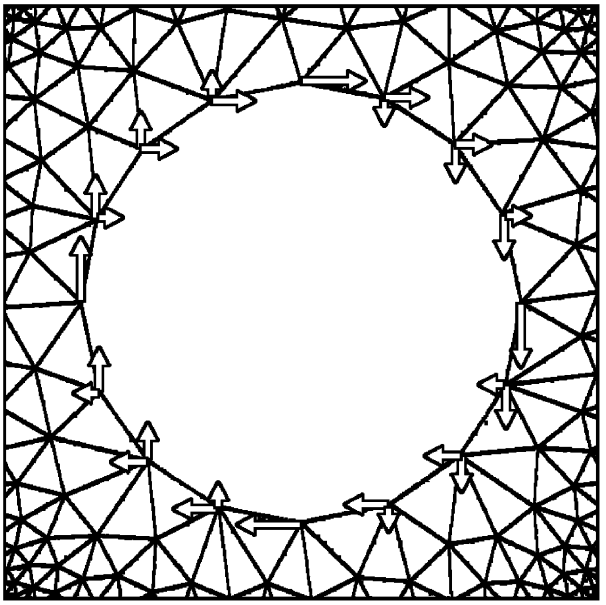

Fig. 9. Effective torque applied to the inner surface of the lamination.

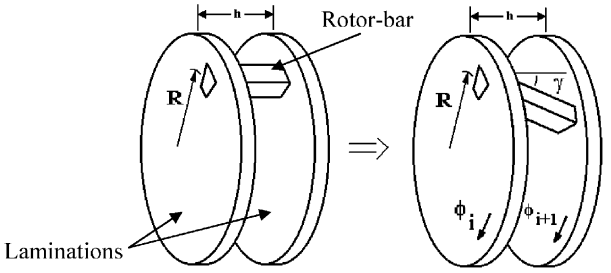

Fig. 10. Relative displacement of two laminations and the deformation of a rotor-bar segment.

where G is the shear modulus [14]. For small deformation, $\delta \approx h\gamma$, where h is the distance between the centers of adjacent laminations. Also, note that the shear stress is related to shear force, F, and the cross-sectional area, A, by $F = A\tau$. Thus,

$$F = \frac{GA}{h}\delta. \tag{3}$$

For a small relative displacement, $\delta = R(\phi_{i+1} - \phi_i)$, and $T_{\text{rel}} = RF$, where T_{rel} is the relative torque between two laminations and R is the distance from the lamination center to the centroid of the rotor-bar cross-section. Finally, the relation between torque and angular displacement for one rotor-bar is

$$T_{\text{rel}} = \frac{GAR^2}{h}\left(\phi_{i+1} - \phi_i\right). \tag{4}$$

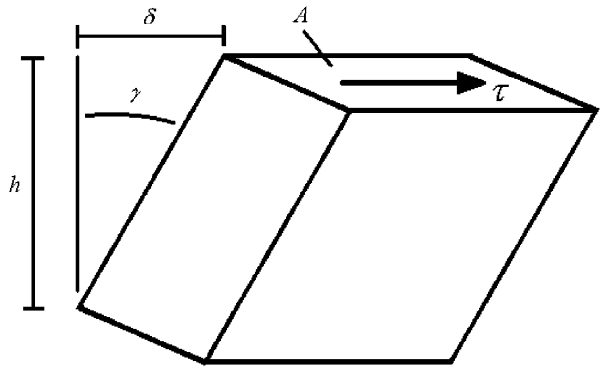

Fig. 11. Segment of a rotor-bar deformed in shear.

The effective torsional stiffness of all the rotor-bars combined is

$$k_{\text{bar}} = N_{\text{bar}} \frac{GAR^2}{h}, \tag{5}$$

where N_{bar} is the number of rotor-bars. For the motor used in the experimental apparatus, the required dimensions are estimated as $A \approx 1.89 \times 10^{-4}\,\text{m}^2$, $R \approx 0.0895\,\text{m}$, and for the 26 gage steel laminations $h = 4.76 \times 10^{-4}\,\text{m}$.

To derive the equations of motion for the compliant model, depicted in Fig. 7, Lagrange's equations are employed:

$$\frac{\mathrm{d}}{\mathrm{d}t}\frac{\partial(T-V)}{\partial \dot{q}_i} - \frac{\partial(T-V)}{\partial q_i} = Q_i, \tag{6}$$

where T and V are the kinetic and potential energy, respectively, and Q_i are the generalized forces corresponding to the generalized coordinates, q_i.

The system kinetic energy is the sum of contributions from the shaft, the laminations, and the connection hardware;

$$T = T_{\text{shaft}} + T_{\text{lam}} + T_{\text{hardware}}. \tag{7}$$

Similarly, the potential energy has contributions from the shaft, the springs connecting the laminations to the shaft and each other, and the torque transducer;

$$V = V_{\text{shaft}} + V_{\text{lam}} + V_{\text{trans}}. \tag{8}$$

For a uniform shaft, the kinetic and potential energies are

$$T_{\text{shaft}} = \frac{1}{2}\rho J \int_0^L \left(\frac{\partial\theta}{\partial t}\right)^2 \mathrm{d}x, \tag{9}$$

and

$$V_{\text{shaft}} = \frac{1}{2} GJ \int_0^L \left(\frac{\partial\theta}{\partial x}\right)^2 \mathrm{d}x, \tag{10}$$

where ρ is the mass density, G is the shear modulus, and J is the polar moment of inertia of the shaft cross-section [15].

The kinetic energy of the disks representing the laminations is

$$T_{\text{lam}} = \frac{1}{2}\sum_{i=1}^{N_{\text{lam}}} I_{\text{lam}}\dot{\phi}_i^2, \tag{11}$$

where ϕ_i is the angular displacement of each lamination, I_{lam} is the moment of inertia of each lamination, and N_{lam} is the number of laminations. The potential energy of the springs connecting the laminations to the shaft and to each other can be expressed as

$$V_{\text{lam}} = \frac{1}{2}\sum_{i=1}^{N_{\text{lam}}} k_{\text{lam}}\big(\theta(x_i) - \phi_i\big)^2 + \frac{1}{2}\sum_{i=1}^{N_{\text{lam}}-1} k_{\text{bar}}\big(\phi_{i+1} - \phi_i\big)^2, \tag{12}$$

where x_i is the position of each lamination along the shaft, and k_{lam} is the stiffness of the lamination found using finite element analysis.

Since the connection hardware is attached to the shaft at $x = L$, its kinetic energy is

$$T_{\text{hardware}} = \frac{1}{2} I_{\text{hardware}}\dot{\theta}^2(L, t), \tag{13}$$

where I_{hardware} is the moment of inertia of the connection hardware. Finally, the torque transducer is connected to both the flywheel and the connection hardware, but the flywheel is fixed. Thus, the potential energy stored in the torque transducer is

$$V_{\text{trans}} = \frac{1}{2} k_{\text{trans}}\theta^2(L, t), \tag{14}$$

where k_{trans} is the torsional stiffness of the torque transducer.

The strain and kinetic energies for the shaft are discretized using the method of assumed modes [16]. To this end the shaft rotation is written as

$$\theta(x, t) = \sum_{i=0}^{N-1} \psi_i(x) p_i(t), \tag{15}$$

where $\psi_i(x)$ are a set of trial functions that satisfy geometric boundary conditions, $p_i(t)$ are a set of generalized coordinates for the shaft rotation, and N is the number of trial functions. The assumed trial functions are chosen to be the natural modes of a free–free uniform shaft,

$$\psi_i(x) = \cos\left(\frac{\mathrm{i}\pi x}{L}\right). \tag{16}$$

Substitution of Eq. (15) into Eqs. (9)–(14) yields

$$T_{\text{shaft}} = \frac{1}{2}\sum_{j=0}^{N-1}\sum_{k=0}^{N-1} \rho J \int_0^L \psi_j\psi_k \,\mathrm{d}x\, \dot{p}_j\dot{p}_k, \tag{17}$$

$$V_{\text{shaft}} = \frac{1}{2}\sum_{j=0}^{N-1}\sum_{k=0}^{N-1} GJ \int_0^L \psi_j'\psi_k' \,\mathrm{d}x\, p_j p_k, \tag{18}$$

$$T_{\text{lam}} = \frac{1}{2}\sum_{i=1}^{N_{\text{lam}}} I_{\text{lam}}\dot{\phi}_i^2, \tag{19}$$

$$V_{\text{lam}} = \frac{1}{2}\sum_{j=0}^{N-1}\sum_{k=0}^{N-1}\sum_{i=1}^{N_{\text{lam}}} k_{\text{lam}}\psi_j(x_i)\psi_k(x_i)p_j p_k + \frac{1}{2}\sum_{i=1}^{N_{\text{lam}}} k_{\text{lam}}\phi_i^2 + \sum_{j=0}^{N-1}\sum_{i=1}^{N_{\text{lam}}} -k_{\text{lam}}\psi_j(x_i)p_j\phi_i + \frac{1}{2}\sum_{i=1}^{N_{\text{lam}}-1} k_{\text{bar}}\phi_i^2 + \frac{1}{2}\sum_{i=1}^{N_{\text{lam}}-1} k_{\text{bar}}\phi_{i+1}^2 + \sum_{i=1}^{N_{\text{lam}}-1} -k_{\text{bar}}\phi_i\phi_{i+1}, \tag{20}$$

$$T_{\text{disk}} = \frac{1}{2}\sum_{j=0}^{N-1}\sum_{k=0}^{N-1} I_{\text{disk}}\psi_j(L)\psi_k(L)\dot{p}_j\dot{p}_k, \tag{21}$$

$$V_{\text{trans}} = \frac{1}{2}\sum_{j=0}^{N-1}\sum_{k=0}^{N-1} k_{\text{trans}}\psi_j(L)\psi_k(L)p_j p_k, \tag{22}$$

where $\psi' = \mathrm{d}\psi/\mathrm{d}x$.

To find the generalized forces acting on the rotor system, it is assumed that the electromagnetic torque is applied uniformly to each of the laminations. Thus, for an applied torque, P_{app}, distributed equally among the laminations, the virtual work is

$$\delta W = \sum_{i=1}^{N_{\text{lam}}} \frac{P_{\text{app}}}{N_{\text{lam}}}\delta\phi_i, \tag{23}$$

where $\delta\phi_i$ is the virtual displacement of the ith lamination. From Eq. (23), the generalized forces are

$$Q_i = \frac{P_{\text{app}}}{N_{\text{lam}}} \tag{24}$$

for each generalized coordinate corresponding to a lamination displacement.

Substitution of Eqs. (17)–(22) and (24) into Eqs. (7) and (8), and substituting the result into Eq. (5) generates equations of motion of the form

$$M\,\underline{\ddot{x}} + K\,\underline{x} = \underline{f}\,, \tag{25}$$

where M and K are the mass and stiffness matrices, respectively. The vector $\underline{x}$ contains the generalized coordinates, p_i and ϕ_i, and the vector $\underline{f}$ contains the generalized forces.

3.2. Rigid rotor model

A sketch of the rigid rotor model appears in Fig. 12. The model consists of two lumped masses and two torsional springs. The first lumped mass, of mass moment of inertia I_1, represents the bulk of the rotor. The torsional spring, of stiffness k_1, models the segment of shaft to the right of the rotor laminations, and to the left of the connection hardware. The connection hardware is lumped together to form I_2. Finally, the torque transducer is represented by a torsional spring, k_2. On the test rig, the torque transducer is

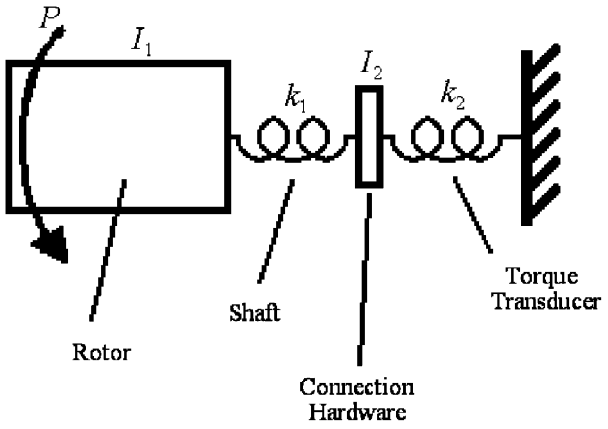

Fig. 12. Schematic of the rigid rotor model.

connected to the flywheel on the right, as shown in the figure, but the flywheel is assumed to be stationary. Thus, the spring k_2 is fixed on the right. The equations of motion for this system are

$$I_1\ddot{\theta}_1 + k_1\theta_1 - k_1\theta_2 = P,$$
$$I_2\ddot{\theta}_2 - k_1\theta_1 + (k_1 + k_2)\theta_2 = 0, \tag{26}$$

where θ_1 and θ_2 are the angular displacements of I_1 and I_2, respectively, and P is the torque applied to the rotor, I_1.

4. Comparison of model and experiment

To compare the compliant and rigid-body models to the experiment and each other, the models are used to predict the response of the connection hardware, based on the measured applied torque. This is achieved by a frequency domain multiplication of the applied torque with the impulse response functions for both torsional models.

For zero damping, the impulse response functions of the rigid body and compliant models are plotted in Fig. 13. The natural frequencies of the first eight modes are listed in Table 1. The responses matches at low frequencies, when the rotor is behaving as a rigid body. However, at higher frequencies, the level of response from the compliant model is higher. This is due to the presence of modes that involve deformation of the rotor.

To make the models more realistic, damping is added to both models. Stiffness-proportional viscous damping is used for this purpose. The equations of motion are modified to have the form

$$M\,\underline{\ddot{x}} + C\,\underline{\dot{x}} + K\,\underline{x} = \underline{f}\,, \tag{27}$$

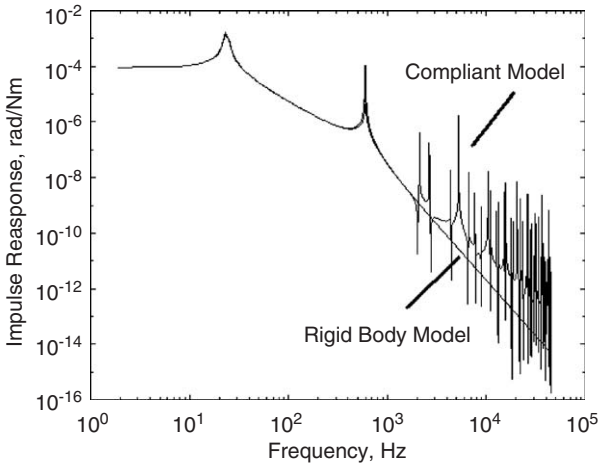

Fig. 13. Impulse response functions of the undamped rigid rotor and compliant rotor models.

Table 1
Mode numbers and natural frequencies for the compliant rotor model

Mode number	Frequency (Hz)
1	24
2	590
3	2107
4	2653
5	4367
6	5255
7	6592
8	7673

where C is a damping matrix such that $C = \beta K$ and β is scalar. With this representation the damping ratio in the nth mode is given by

$$\varsigma_n = \frac{\beta \omega_n}{2}, \tag{28}$$

where ω_n is the natural frequency of the nth mode in rad/s.

For a damping value of $\beta = 0.001$, which translates into a damping ratio of $\zeta = 0.015$ for the first mode, the impulse response functions for both torsion models are plotted in Fig. 14. The response of the compliant model at high frequencies is still higher than that of the rigid-body model, even though the resonance peaks have been damped out.

Multiplying the damped frequency response functions, of Fig. 14, by the measured applied torque, shown in Fig. 5, results in two predictions of the connection hardware response during the experiment. These two predictions and the measured response are plotted in Fig. 15. The compliant rotor model provides a better prediction of the high-frequency response; the response

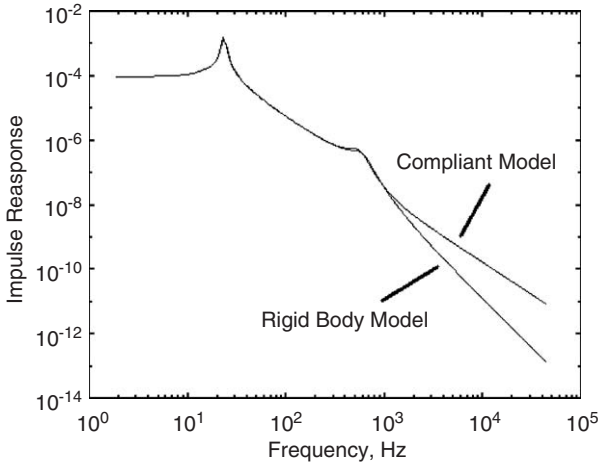

Fig. 14. Impulse response functions of the rigid rotor and compliant rotor models, with a damping ratio in the first mode of $\zeta = 0.015$.

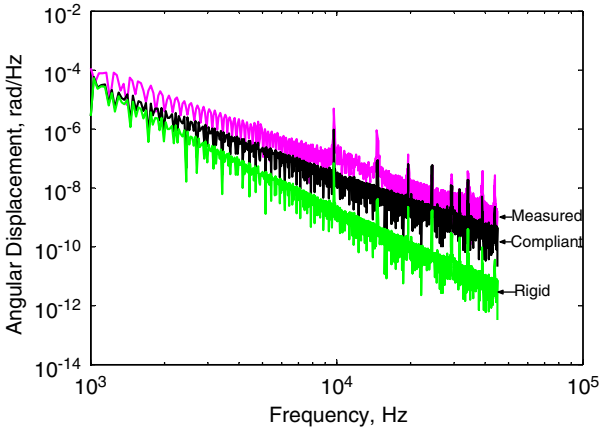

Fig. 15. Measured and predicted responses of the connection hardware for a fundamental frequency of 20 Hz and $\zeta = 0.015$.

peaks of the compliant model are slightly less than measured, while that for the rigid-body model significantly underestimates the response.

A simulation was performed to study the influence of varying the drive switching frequency. For computational expediency the standard q–d model [17] was used to simulate the input torque to the compliant motor model with zero damping. Fig. 16 shows a surface plot the connection hardware response as a function of frequency and switching frequency, where lighter colors indicate a larger response. The vertical line is a natural frequency of the system, and the diagonal lines are switching harmonics. When a switching harmonic matches a natural frequency of the model, the response amplitude increases dramatically. This reinforces the need to have an

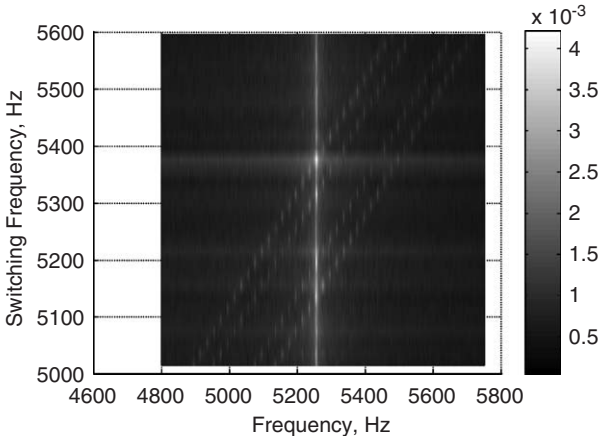

Fig. 16. Surface plot of the magnitude of the connection hardware deflection as a function of frequency and switching frequency using the standard q–d model—the colors indicate the amplitude of the response in rad/Hz. The vertical line is a natural frequency of the system. The diagonal lines are switching harmonics.

accurate model at high frequency, to ensure that natural frequencies are not excited by switching harmonics.

5. Conclusions

When constructing a model to study the high-frequency vibration of electric machinery in torsion, it is critical to include compliance of the rotor. Otherwise, an accurate prediction of the high-frequency response cannot be made. The commonly used rigid rotor model will underestimate the high-frequency response of the system. Further, it is important to know the high-frequency dynamics of the system in order to avoid a resonance condition when a switching harmonic matches a natural frequency.

The compliant induction motor model presented here is an improvement over the rigid-body model typically used. It is adequate for demonstrating the importance of including compliance in the rotor when studying high-frequency response. However, it may be improved by further investigation of the deformation and friction mechanisms at work in the rotor. These factors must be understood in order to give a designer a model that can be used to manipulate the high-frequency torsional response of an induction motor.

Acknowledgements

This research was supported by the Office of Naval Research under grant number N00014-98-1-01716, "High Frequency Vibration Analysis of Electric Machinery." The authors would also like to thank Brian T. Kuhn and Dr. Patrick L. Chapman for their help with the experimental and modeling work.

References

[1] K.G. Bush, *Electrical Variable Speed Drives*, Blackwell Science, Oxford, 1995.

[2] D.J. Sheppard, Torsional vibration resulting from adjustable-frequency AC drives, *IEEE Transactions on Industry Applications* 24 (5) (1988) 812–817.

[3] C. Wang, J.C.S. Lai, Vibration analysis of an induction motor, *Journal of Sound and Vibration* 224 (4) (1999) 733–756.

[4] P. Calonnec, T. Derrey, E. Destobbeleer, L. Protin, Induction motor mechanical failure: influence of the converter on torque pulsation, *Seventh International Conference on Electrical Machines and Drives*, University of Durham, UK, September 11–13, 1995, pp. 136–140.

[5] Y.-N. Wang, J.-C. Gu, C.-M. Chen, Analysis of the torsional vibration of an induction motor supplied by distorted voltage sources, *Journal of the Chinese Institute of Electrical Engineering* 6 (2) (1999) 87–97.

[6] C.-O. Hong, S.-K. Sul, Analysis of shaft torsional vibration in inverter-fed induction motor drive systems, *Conference Record—IAS Annual Meeting (IEEE Industrial Applications Society)*, Vol. 1, IEEE, Piscataway, NJ, 1993, pp. 588–594.

[7] M. Perrin, G. Kohn, S. Mugford, G. Seggewiss, Induction motors, reciprocating compressors and variable frequency drives, *Record of Conference Papers—Annual Petroleum and Chemical Industry Conference*, IEEE, Piscataway, NJ, 1997, pp. 1–9.

[8] J.R. Shadley, B.L. Wilson, M.S. Dorney, Unstable self-excitation of torsional vibration in AC induction motor driven rotational systems, *Journal of Vibration and Acoustics* 114 (1992) 226–231.

[9] Y.-S. Kim, S.-B. Kim, J.-S. Kim, C.-H. Yoo, H.-J. Kim, Two-degree-of-freedom speed control of induction motor having two-mass resonant system, *IECON Proceedings (Industrial Electronics Conference)*, Vol. 2, 1996, pp. 1210–1215.

[10] J.-S. Kim, Y.-S. Kim, J.-H. Shin, H.-J. Kim, *H* infinity speed control of an induction motor with the two-mass resonant system by LMI, *IECON Proceedings (Industrial Electronics Conference)*, Vol. 3, 1998, pp. 1439–1444.

[11] M. Mine, K. Date, H. Ohmori, A. Sano, Y. Todaka, H. Nishida, New simple adaptive control subject to disturbances and application to torsional vibration suppression, *Proceedings of the 1999 IEEE International Conference on Control Applications, Hawaii*, August 22–27, 1999, pp. 521–526.

[12] S.D. Sudhoff, P.L. Chapman, B.T. Kuhn, D. Aliprantis, An advanced induction machine model for predicting inverter-machine interaction, *IEEE Transactions on Energy Conversion* 17 (2) (2002) 203–210.

[13] S.D. Sudhoff, D.C. Aliprantis, B.T. Kuhn, P.L. Chapman, Experimental characterization procedure for use with an advanced induction machine model, *IEEE Transactions on Energy Conversion* 18 (1) (2003) 48–56.

[14] R.R. Craig Jr., *Mechanics of Materials*, Wiley, New York, 1996.

[15] L. Meirovitch, *Principles and Techniques of Vibration*, Prentice-Hall, Upper Saddle River, 1997.

[16] L. Meirovitch, *Computational Methods in Structural Dynamics*, Sijthoff and Noordhoff, Rockville, 1980.

[17] P.C. Krause, O. Wasynczuk, S.D. Sudhoff, *Analysis of Electric Machinery and Drive Systems*, IEEE Press, New York, 1995.